DIFFRACTION-LIMITED IMAGING. II. OPTICAL APERTURE-SYNTHESIS IMAGING OF TWO BINARY STARS

T. Nakajima, S. R. Kulkarni,[a] P. W. Gorham, A. M. Ghez, G. Neugebauer, J. B. Oke, T. A. Prince,
AND A. C. S. Readhead
Palomar Observatory, California Institute of Technology, Pasadena, California 91125
Received 17 January 1989; revised 7 February 1989

ABSTRACT

We have used the technique of nonredundant masking at the Hale 5 m telescope and radio VLBI imaging software to make optical aperture-synthesis maps of two binary stars, β Corona Borealis and σ Herculis. The dynamic range of the map of β CrB, a binary star with a separation of 230 milliarcsec, is about 50:1. For σ Her, we find a map of β CrB, a binary star with a separation of 230 milliarcsec, and the dynamic range of our image is 30:1. These maps demonstrate the potential of the nonredundant masking technique for diffraction-limited imaging of astronomical objects with high dynamic range. We find that the optimal integration time for measuring the closure phase is longer than that for measuring the fringe amplitude. There is not a close relationship between amplitude errors and phase errors, as is found in radio astronomy, and amplitude self-calibration is less effective at optical wavelengths than at radio wavelengths. The primary-beam sensitivity correction made in radio interferometry is not necessary for optical interferometry.

I. INTRODUCTION

Three years ago, we began a concerted program to obtain diffraction-limited images at optical wavelengths using the Hale 5 m telescope of the Palomar Observatory. The basic goal of this program is to understand quantitatively the strengths, limitations, and sensitivities of different high-resolution imaging techniques. The background to this work and the demonstration of the feasibility of constructing diffraction-limited images on the 5 m telescope, using the techniques adapted from radio astronomy, have been described elsewhere (Readhead *et al.* 1988, hereafter referred to as Paper I). We have concentrated our efforts on understanding the tradeoffs between the fully filled aperture (FFA) and nonredundant-masking (NRM) techniques. In this paper we present the first diffraction-limited images obtained by optical aperture synthesis using nonredundant masks on the Hale telescope. In a subsequent paper we will present results obtained using the FFA (Gorham *et al.* 1989). In parallel with these observational efforts, we have embarked on a detailed analytical study of the problems associated with diffraction-limited imaging (Paper I; Nakajima 1988; Kulkarni 1988; Kulkarni and Nakajima 1989; Nakajima *et al.* 1989).

Other groups are engaged in similar studies aimed at exploiting the imaging potential of optical telescopes, and results have been published of a number of high-resolution observations using speckle interferometry (Labeyrie 1972), the Knox–Thompson algorithm (e.g., Nisenson *et al.* 1985), the speckle-masking method (e.g., Hoffman and Weigelt 1986), and the NRM technique (Haniff *et al.* 1987).

Unlike speckle interferometry, which uses full uv coverage with attenuated complex amplitudes, the NRM technique uses limited uv coverage with high signal-to-noise ratio. A detailed study of the tradeoffs between the speckle-masking technique and the nonredundant masking technique shows that the NRM method produces images of higher dynamic range at medium to high light levels, while the speckle masking is better suited to pursuing the faint limit (Kulkarni and Nakajima 1989). Finally, the NRM can

be regarded as a first step towards an optical interferometric array and is important in establishing an optimal image-reconstruction procedure and understanding the potential and limitations of the performance of an interferometric array under the constraint of passive optics.

For our first attempts, only bright binary stars were observed. The reconstructed images demonstrate intrinsically high resolution and potentially high dynamic range. The instrumentation and the observing procedure are described in Secs. II and III. The data reduction and analysis are found in Sec. IV. Images of binary stars are presented in Sec. V along with the discussion of their dynamic range. In Sec. VI, the image-reconstruction procedure and the estimation of the dynamic range are re-examined and distinctions between radio interferometry and optical interferometry are discussed in detail.

II. INSTRUMENTATION

A schematic drawing of the optics of the prime-focus camera for the Hale 5 m telescope is shown in Fig. 1. An $f/3.3$ primary beam is collimated by a Nikon $f/2.8$ 85 mm camera lens. The lens forms an image of the primary mirror at a distance of about 85 mm (1 focal length), where a mask is placed on a stepper-motor-driven rotary stage controlled by a personal computer. One millimeter on the mask plane is equivalent to 19.8 cm on the primary mirror. Another camera lens identical to the first forms a second focus, where the scale is 12″/mm. The image is expanded by a microscope objective with a power of 80. The final image size on the detector is 0.15″/mm. A 6300 Å interference filter with 30 Å bandpass was set between the microscope objective and the detector throughout the run.

The detector is a resistive-anode, position-sensing, photon-counting detector (ITT #FM 4146M). It has a MA-2 photocathode, essentially a red extended S-20, and five stages of microchannel plates (MCPs) arranged in a V–Z configuration. A net potential drop of about 5 kV is maintained from the cathode to the anode. Each primary photoelectron results in an avalanche of 10^7–10^8 secondary electrons onto the resistive anode. Output currents from the four corners of the resistive anode are amplified and fed to an

[a] Presidential Young Investigator and Alfred P. Sloan Fellow.
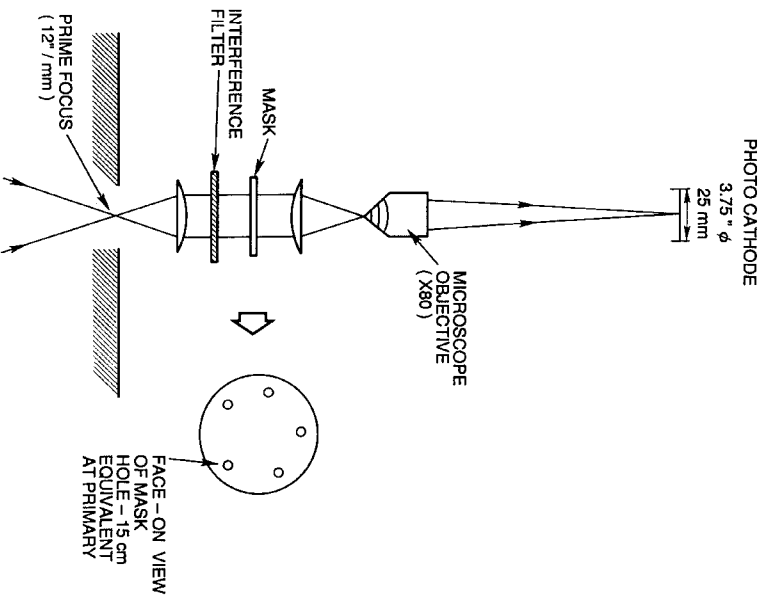
FIG. 1. Schematic of the optics of the prime-focus camera. A mask is placed at the image of the primary mirror made by the collimator lens.

analog-to-digital position computer (Surface Science Lab, Mountain View, CA), which converts input currents into (x,y) coordinates of the avalanche. The position computer outputs 10 bits per axis as well as a strobe pulse; the position conversion takes approximately 10 μs, and this is a source of one of the deadtimes of the detector. Another source of deadtime is the charge depletion resulting from the large gain of the tube. This has the effect that after an avalanche of secondary electrons, the pixel(s) corresponding to the location of the photoelectron are dead, for perhaps as long as several tens of milliseconds. Fortunately, for our case the fringes spread the light out and, for the counting rates reported in this paper ($< 1.5\times10^4$ s^{-1}), deadtime effects were negligible. A camera interface appended 12 bits of arrival-time information to the photon coordinate data and passed the resulting "event" to a Digital Equipment Corporation (DEC) μVax workstation via a DEC DRV-11 parallel interface. At appropriate times, the interface unit also sends the absolute time (32 bits) to the computer, enabling a reconstruction of the absolute arrival time of each photon to better than 1 μs. The data were first recorded onto a hard disk of the μVax and later transferred to a magnetic tape for archival storage and processing.

In order to decrease the dark current, the detector was cooled to $-20\,°$C with liquid nitrogen. At this temperature, the dark-count rate was below 20 counts s^{-1} over the entire area of the detector. By comparing the actual count rate of stars of known magnitudes, the net throughput of the observing system was inferred to be 0.7%. This is determined primarily by the net detector efficiency of about 2% and the filter transmittance of 40%. The nominal spatial resolution of the detector is 60 μm FWHM and the size of the active area is 25 mm in diameter. The corresponding angular resolution and field of view are 9 milliarcsec (mas) FWHM and 3.75" in diameter, respectively. The spatial linearity was tested by measuring an artificial fringe pattern in the laboratory and the nonlinearity was found to be negligible.

III. OBSERVING PROCEDURE

Observations were made over the nights of 3 and 4 April 1988. Objects near the zenith were selected to minimize the path length in the atmospheric layer. The seeing condition varied between 1" and 2.5" during the run. Observations of the binary stars whose images were successfully reconstructed were made under 1.5" visual seeing or better. A nearby point-source calibrator was observed for each binary star with the same uv coverage. Observations of a program source and the corresponding calibrator were separated in time by less than 30 min.

Two kinds of masks were used depending on the necessary resolution and uv coverage. One was a five-hole mask which had relatively short baselines and a uniform uv coverage at each position angle. The maximum baseline length of this mask was 220 cm. The other was a six-hole mask which had three widely separated pairs of holes. Each pair formed a short baseline of about 40 cm. The pairs were separated by about 280 cm and the maximum baseline length was 310 cm. The equivalent size of each hole in both masks was 15 cm in diameter on the primary mirror. The observations were made at four or five different rotational angles. The uv coverage of these two masks is shown in Figs. 2 and 5, respectively. For each rotational angle, either $\sim 6\times10^5$ or $\sim 12\times10^5$ events were recorded.

IV. DATA REDUCTION AND ANALYSIS

The data reduction and analysis were carried out on a CONVEX C-1 minisupercomputer and a VAX/780 and consisted of several phases: (i) Determination of spatial frequencies; (ii) Estimation of the fringe amplitude and closure phase; (iii) Calibration of the fringe amplitude, and (iv) Model fitting and hybrid mapping.

a) Determination of Spatial Frequencies

Initially, 10 ms was adopted as a default-coherent integration time frame τ and power spectra of the "frames" were obtained; here a frame is an image obtained over integration time equal to τ. Given the small number of photons per frame, it was computationally advantageous to calculate and integrate the frame autocorrelation functions (ACF) followed by the Fourier transform of the integrated ACF to yield the power spectrum.

The purpose of calculating the power spectrum was to determine the spatial frequencies provided by the mask. In principle, the spatial frequencies could have been measured by measuring accurately the coordinates of the holes in the mask if the alignment of the optics had been perfect. Instead, however, we inferred the spatial frequencies from the integrated power spectrum of observed data.

Approximate spatial frequencies of fringes were obtained by centroiding power-spectrum components which had finite extent in the spatial-frequency domain. In a mask with n_s holes, only $n_s - 1$ hole coordinates must be determined since the origin of the mask plane is arbitrary. Least-squares fitting was therefore made to determine $n_s - 1$ unknown hole coordinates from $n_s(n_s - 1)/2$ power peaks. The n_s

hole coordinates were pairwise differenced to yield $n_s(n_s-1)/2$ baseline vectors. This procedure ensured that all the triangles closed (see below).

From the knowledge of the focal lengths and magnification of the optics, the baseline vectors were converted from pixel units to spatial-frequency units. The absolute errors in the measurement of the baseline vectors in the detector plane are determined by the signal-to-noise ratio of the power spectrum, while the systematic error in the conversion of the baseline vectors to spatial frequencies depends on the precision of alignment of the optics. It was found that the systematic error of 3% in scaling dominated the errors in the spatial frequencies. The orientation of the detector on the sky was determined from a low-magnification image of a globular cluster core. The position angle towards north was estimated to be precise to 1°.

b) Estimation of the Fringe Amplitude and Closure Phases

Once the spatial frequencies were determined, it was computationally advantageous to evaluate the discrete Fourier transform (DFT) of the raw data at those frequencies and to estimate the bispectrum or the triple product at only selected spatial-frequency triplets.

The DFT was evaluated at the spatial frequencies derived earlier from the power-spectrum data in each frame. The DFT component at a spatial frequency $\mathbf{u}$ of the jth frame $\tilde{D}_j(\mathbf{u})$ is given by

$$\tilde{D}_j(\mathbf{u}) = \sum_{k=1}^{N_j} \exp(i\mathbf{u}\cdot\mathbf{x}_k),$$ (1)

where N_j is the number of photons in the jth frame and $\mathbf{x}_k$ is the location of the k th event. An unbiased estimator of the classical power spectrum for the jth frame is given by

$$\tilde{Q}_j^{(2)}(\mathbf{u}) = |\tilde{D}_j(\mathbf{u})|^2 - N_j$$ (2)

(Goodman and Belsher 1976,1977; Dainty and Greenaway 1979). An unbiased estimator of the classical bispectrum for the jth frame, $\tilde{Q}_j^{(3)}(\mathbf{u}_1,\mathbf{u}_2)$, is given by

$$\tilde{Q}_j^{(3)}(\mathbf{u}_1,\mathbf{u}_2) = \tilde{D}_j(\mathbf{u}_1)\tilde{D}_j(\mathbf{u}_2)\tilde{D}_j^{(3)}(-\mathbf{u}_1-\mathbf{u}_2)$$
$$- [|\tilde{D}_j(\mathbf{u}_1)|^2 + |\tilde{D}_j(\mathbf{u}_2)|^2$$
$$+ |\tilde{D}_j(-\mathbf{u}_1-\mathbf{u}_2)|^2 - 2\tilde{N}_j]$$ (3)

(Wirnitzer 1985).

The determination of spatial frequencies by centroiding power-spectrum components is not necessarily free from error. This can result in a nonclosing triplet of spatial frequencies which introduces a complex photon-noise bias in the bispectrum. Suppose three fringe frequencies $\mathbf{u}_1$, $\mathbf{u}_2$, and $\mathbf{u}_3$ satisfy the closure relation only approximately as

$$\mathbf{u}_1 + \mathbf{u}_2 + \mathbf{u}_3 = \mathbf{w},$$ (4)

where w is a small but nonzero residual spatial frequency and $|\mathbf{w}\cdot\mathbf{x}_k| \ll 1$. The triple product of the three DFT components is

$$\tilde{D}_j(\mathbf{u}_1)\tilde{D}_j(\mathbf{u}_2)\tilde{D}_j(\mathbf{u}_3)$$
$$= \tilde{D}_j(\mathbf{u}_1)\tilde{D}_j(\mathbf{u}_2)\tilde{D}_j(-\mathbf{u}_1-\mathbf{u}_2) + i\tilde{D}_j(\mathbf{u}_1)\tilde{D}_j(\mathbf{u}_2)\mathbf{w}$$
$$\times \sum_{k=1}^{N_j} \mathbf{x}_k \exp[i(-\mathbf{u}_1-\mathbf{u}_2)\cdot\mathbf{x}_k],$$ (5)

where $\exp(i\mathbf{w}\cdot\mathbf{x}_k) \simeq 1 + i\mathbf{w}\cdot\mathbf{x}_k$ was used. The additional term

$$i\tilde{D}_j(\mathbf{u}_1)\tilde{D}_j(\mathbf{u}_2)\sum_{k=1}^{N_j}\mathbf{w}\cdot\mathbf{x}_k\exp[i(\mathbf{u}_1+\mathbf{u}_2)\cdot\mathbf{x}_k],$$

which equals

$$\tilde{D}_j(\mathbf{u}_1)\tilde{D}_j(\mathbf{u}_2)\mathbf{w}\cdot\nabla_{\mathbf{u}_1+\mathbf{u}_2}\tilde{D}_j(-\mathbf{u}_1-\mathbf{u}_2),$$ (6)

introduces a complex bias in the measured bispectrum. In principle, this bias can be taken into account provided w is known. The closure relation through the least-squares fitting was used to adjust the spatial frequencies and thus to ensure $\mathbf{w} = 0$, eliminating the need for the additional bias compensation. Squares of unbiased estimators were also integrated to determine variances. These are used in the computation of the signal-to-noise ratio. After integration, mean fringe amplitudes were obtained from the power spectrum normalized by the zero-frequency component, and mean closure phases were obtained from bispectral components along with their signal-to-noise ratios.

In order to obtain the maximum signal-to-noise ratio, DFTs were taken with different integration times ranging from 10 to 100 ms for a dataset taken at one rotational angle of the mask for each object. Since the decorrelation caused by the atmospheric disturbance is continuous, there is no physical frame boundary. For this reason, frames were over-sampled and each photon was processed twice. As a result of oversampling, the final signal-to-noise ratio increased by 30%-40% compared to the case without oversampling and thus the procedure was justified. For the observations of the binary stars presented in this paper, the optimal integration time was found to be around 20 ms. The behavior of the fringe amplitude, signal-to-noise ratios of the fringe amplitude, signal-to-noise ratio and closure phase as functions of integration time is discussed in detail in Sec. VI.

c) Calibration of the Fringe Amplitude

The method of choice for the amplitude calibration depends on the timescale of the calibration and the nature of dominant errors. As an analogy to radio interferometry, we first considered an application of amplitude self-calibration. However, it was found to be difficult to carry out amplitude self-calibration in optical interferometry, and this difficulty is discussed in Sec. VI.

An attempt to correct long-term and static systematic errors was made by dividing fringe amplitudes of objects by those of corresponding point-source calibrators. The extent to which this correlation works depends on the stability of systematic errors. For one of the two binary stars whose images are presented here, the correction was fairly successful and for the other binary star it was less successful. (Sec. V).

d) Model Fitting and Hybrid Mapping

So far, photon coordinates with arrival times were reduced to calibrated fringe amplitudes and closure phases. The image construction was done using the Caltech VLBI hybrid-mapping package (Pearson and Readhead 1984) in two steps: (a) the best-fit model was obtained by direct model fitting to the observables; and (b) the final image was obtained by using the observables and the model as inputs to the hybrid mapping.

The input model for hybrid mapping was derived by a

least-squares fitting of a model binary star with the calibrated fringe amplitude and closure phases. A nonlinear model-fitting program of the software package was used with some minor modifications. The modification consisted of changing the relative weights of the closure phase and amplitudes. This was done because in the VLBI software package the number of independent closure phases is assumed to be $(n_s - 1)(n_s - 2)/2$, which is true in a regime of high signal-to-noise ratio, as in radio interferometry. This number is actually the number of mathematically independent phases in error-free phase-closure relations. However, data are always corrupted by finite errors and what is really relevant for model fitting is the number of statistically independent closure phases. As shown by Kulkarni (1988) for the Gaussian-noise regime and Kulkarni and Nakajima (1989) for the Poisson regime, the number of statistically independent closure phases increases from $(n_s - 1)(n_s - 2)/2$ to $n_s(n_s - 1)(n_s - 2)/6$ as the signal-to-noise ratios of the closure phases decrease. In optical interferometry, it can safely be assumed that all the $n_s(n_s - 1)(n_s - 2)/6$ closure phases are independent, since their signal-to-noise ratios per short exposure frame are generally very low (<0.1). The relative statistical weighting between the χ^2 of the fringe amplitude and the χ^2 of the closure phase was adjusted by increasing the weight of the χ^2 of the closure phase by $\{[n_s(n_s - 1)(n_s - 2)/6]/n_s(n_s - 1)/2\} = n_s/3$.

A hybrid-mapping procedure was carried out in a single pass without iterations, because of the simplicity of the source structure. The major purposes of hybrid mapping were to obtain a true image with an estimate of dynamic range, to correct for any residual station-dependent amplitude errors, and to look for any additional features of the object.

In order to synthesize the image from the uv data, closure phases must be reduced to fringe phases. Closure-phase relations were algebraically solved with the aid of the model phases (Readhead and Wilkinson 1978). The amplitudes were then adjusted by self-calibration using the method of Cornwell and Wilkinson (1981). However, as discussed in Sec. VI, baseline-dependent errors seemed to be significant at optical wavelengths and the effectiveness of amplitude self-calibration was questionable.

Finally, the Fourier inversion was carried out. Based on the calibrated amplitudes and derived phases, a dirty map and a dirty beam were computed, and the final deconvolution was done using the CLEAN algorithm (Högbom 1974).

V. RESULTS

We have fully reduced three binary stars, β Corona Borealis, σ Herculis, and β Leonis Minoris. All of them have been studied by speckle interferometry (McAlister and Hartkopf 1984, and references therein). We report the successful imaging of the first two and failure in the third.

β CrB. This is a spectroscopic binary with visual magnitude ≈ 3.7 mag (Hoffleit and Jaschek 1982). It has been continuously studied by speckle interferometry since 1973, and the separation ranged from 40 to 310 mas (McAlister and Hartkopf 1984).

Observations of this system were made on the night of 3 April 1988, using the five-hole mask at four different rotational angles. The seeing was about 1". The uv coverage is shown in Fig. 2. 1.2×10^6 photons were recorded at a rate of 5.7 kHz for each rotational angle. For an integration time of 20 ms, there were 114 photons per frame and 2.1×10^5
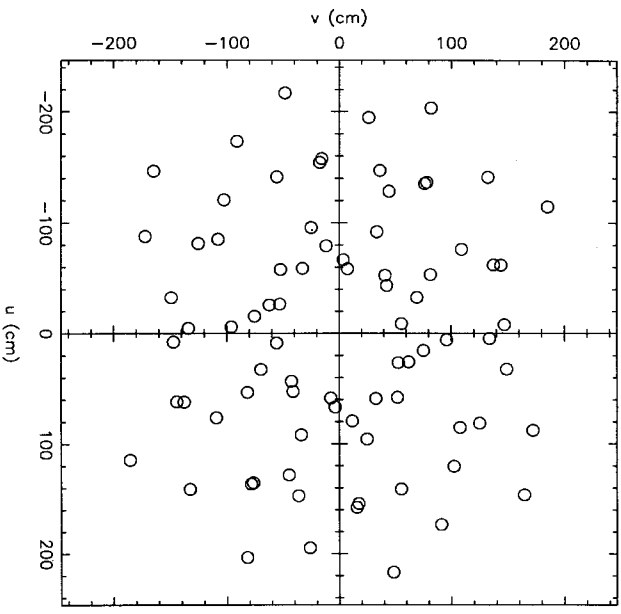

FIG. 2. uv coverage for the observation of β CrB. The unit is not wavelength as usual, but baseline length in centimeters.

frames in all, because of the oversampling by a factor of 2. Fringe amplitudes were calibrated by using observations of δ Boötis. The raw fringe amplitudes of the object and the calibrator, and the calibrated fringe amplitude, are plotted against the projected uv plane along the orientation of the binary in Fig. 3. The upper bound of the raw fringe amplitude of the calibrator is about 50%. This is consistent with Monte Carlo simulations of an atmospheric phase screen based on a Kolmogorov spectrum which give an average fringe amplitude of 60% under a condition of 1" seeing (Nakajima et al. 1989). For the NRM with 15 cm holes, the diffractive effect which degrades the wave front across the aperture and the refractive effect which causes wandering of the Airy disk appear to be equally significant in reducing the fringe amplitude according to the results of the simulations. A clear modulation in the calibrated fringe amplitude demonstrates the success of the empirical calibration procedure. There were 40 fringe amplitudes and 40 closure phases. Examples of closure phases and their signal-to-noise ratios are shown in Table I. The average signal-to-noise ratios of the amplitudes and the closure phases were 25 and 8, respectively. We expect that the signal-to-noise ratio in the map will be limited by that of the closure phase and approximated by $8 \times \sqrt{40} = 50$.

The reconstructed image is shown in Fig. 4. A binary system with $\Delta m = 1.49$ mag, P.A. $= +138°.5$, and $\Delta\theta = 231$ mas was well resolved by a beam of 50 mas FWHM. As was mentioned earlier, the P.A. is good to 1° because of the systematic error in the determination of the orientation in the sky. The largest spurious component is -2% of the maximum. The dynamic range defined as the ratio between the maximum and the largest spurious component is about 50:1, which is consistent with the signal-to-noise ratio of the closure phases, as discussed above.

α Her. This is a double-line spectroscopic binary with a visual magnitude of 4.2 mag. It was first discovered to be a
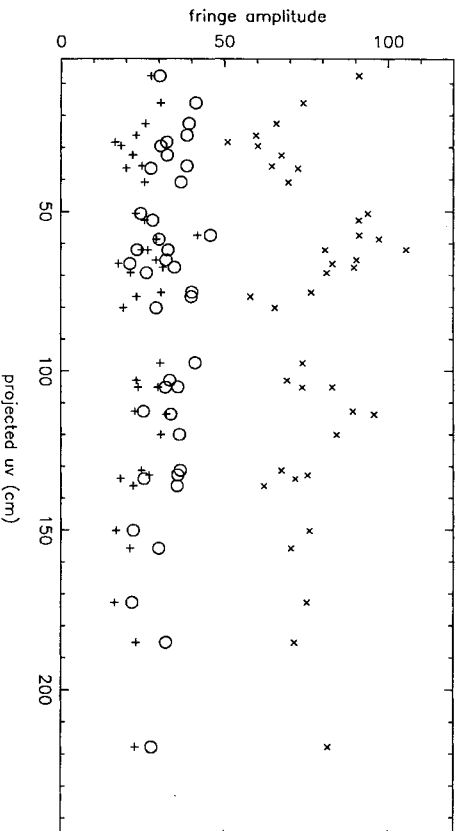
FIG. 3. Raw fringe amplitudes of β CrB (+), and calibrated raw fringe amplitudes of δ Boo (○), are plotted against the projected uv plane along the orientation of the binary.

binary by speckle interferometry in 1972 and the separation ranged from <30 (unresolved) to 119 mas (McAlister and Hartkopf 1984).

The observation was made on 4 April 1988, using the six-hole mask at five different rotational angles. The resultant uv coverage is shown in Fig. 5. 6.0×10^5 photons were recorded at a rate of 4.2 kHz for each rotational angle. The seeing was about 1.5″. For an integration time of 20 ms, there were 84 photons per frame and 1.4×10^5 frames in all. Fringe amplitudes were calibrated by a point source, σ Herculis. The raw fringe amplitudes of the object and the calibrator, and the calibrated fringe amplitude, are plotted against the projected uv plane along the orientation of the binary in Fig. 6. The amplitude calibration of σ Her was not as successful as that

of β CrB. There were 75 fringe amplitudes and one hundred closure phases. The average signal-to-noise ratio of the amplitudes was 13, while that of the closure phases was 5. Thus the expected signal-to-noise ratio in the map is dominated by the closure-phase error and is $5 \times \sqrt{100} = 50$.

The reconstructed image is shown in Figs. 7 and 8 [Plate 79]. A binary system of a separation of 70.5 mas was resolved by a beam of 30 mas FWHM. $\Delta m = 2.36$ mag, P.A. $= -174.4°$. The largest spurious component is 3% of the maximum. The dynamic range is about 30:1, worse than expected from the signal-to-noise ratio of the closure phases or the amplitudes. We suspect that the decrease in dynamic range from the theoretically expected value is due to systematic errors in the calibrated amplitudes.

TABLE I. An example of calibrated data. Calibrated fringe amplitudes and closure phase of β CrB at the position angle of the mask, 144°, are shown along with their signal-to-noise ratios and hole coordinates.

hole number	x-coordinate(cm)	y-coordinate(cm)
1	-125.16	27.80
2	-132.92	175.43
3	4.08	130.56
4	21.82	192.91
5	-36.95	200.48

hole combination	fringe amplitude	SNR
12	0.687	27.5
13	0.507	14.2
14	0.818	20.2
15	0.741	25.3
23	0.695	24.4
24	0.830	29.2
25	0.599	24.8
34	0.715	28.9
35	0.575	24.6
45	0.647	27.2

hole combination	closure phase	SNR
123	10.21	6.6
124	-0.05	7.4
125	7.03	9.2
134	0.34	6.1
135	8.20	6.8
145	4.75	8.4
234	-3.13	9.7
235	14.54	6.9
245	-7.00	9.2
345	-24.12	11.0

y (milliarcsec)

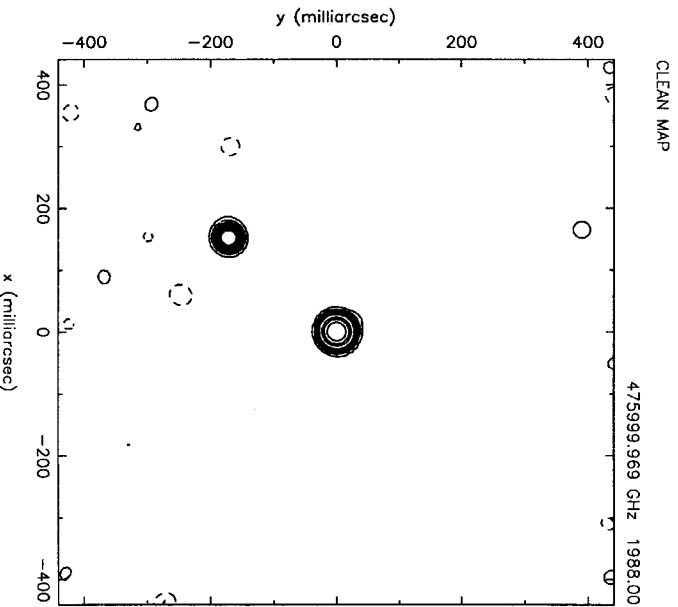CLEAN MAP   475999.969 GHz 1988.00

FIG. 4. Reconstructed image of β CrB. Contour levels are -2%, -1%, 1%, 2%, 3%, 5%, 10%, 20%, 30%, 40%, 50%, and 60% of the maximum. The top is to the north and the left to the east.

was 5 ms and the mean fringe amplitude of the calibrator (ϵ Ursa Majoris), was below 20% for this integration time. The average signal-to-noise ratio of the amplitudes was 12, while that of the closure phases was 2.5. The low average signal-to-noise ratio of the closure phases is due to the poor seeing condition.

Although a map of this binary star has been presented as a preliminary result (Kulkarni 1988a), we were not able to confirm it by the reorganized image-reconstruction procedure described in the previous section. A model fitting only with fringe amplitudes gave $\Delta m = 1.67$ mag and $\Delta \theta = 322$ mas P.A. $= 60^\circ.4$ or $-119^\circ.6$, with a systematic error of $\pm 1^\circ$. The quality of closure phases was too low to determine the orientation uniquely.

VI. DISCUSSION

In this section we first re-examine the image-reconstruction procedure and the estimation of the dynamic range. Then we discuss fundamental differences between radio interferometry and optical NRM.

a) Potential of Hybrid Mapping for Imaging Unknown Sources

Since the objects are known binary stars, we explicitly utilized this fact in the data analysis described in Sec. IV. In order to test the potential for imaging unknown sources, hybrid mapping was carried out for β CrB and σ Her using a point source as a starting input model instead of using the nature of the sources. It was found that hybrid mapping was effective in revealing companions of both of the binary stars and was successful in obtaining the images identical to the ones shown in Sec. V.

In the case of β CrB, the companion appeared as the largest component among positive components, and a negative spurious component was the largest in the CLEAN map after the first iteration. As a common exercise of hybrid mapping, the CLEAN map was used as the input for model fitting, and the best-fit binary star was obtained. Therefore the image identical to that obtained by the procedure described in Sec. IV was constructed in the second iteration. In the case of σ Her, the companion appeared as the largest component in the CLEAN map after the first iteration. Again, model fitting using the CLEAN map as the input gave the best-fit binary star, and the second iteration was identical to the single-path hybrid mapping described in Sec. IV. A point source is a better starting point for σ Her than for β CrB, since the magnitude difference of σ Her is larger.

The success of hybrid mapping using point sources as starting models implies that the NRM can be very sensitive to a faint secondary feature in the presence of a bright point source as a phase reference. For instance, a map of a 10 mag star with a dynamic range of 100 will contain meaningful features to 15 mag. Simulations of imaging more complicated objects are discussed in Paper I. However, a further investigation is necessary based on actual observing data.

b) Examination of Dynamic Range

In Sec. V the dynamic range was defined crudely as the ratio of the maximum and the largest spurious component in the CLEAN map. Another way of estimating the dynamic range is to see the change of the goodness of fit according to the deviation of the model from the best-fit model. In Table II, degrees of freedom and χ^2 are shown for different models

β LMi. This is a double-line spectroscopic binary consisting of a G8 III star with a visual magnitude of 4.2 mag and a F8 V star with a visual magnitude of 6.1 mag (Hoffleit and Jaschek 1982). It has been observed by speckle interferometry since 1975, and the separation has been decreasing from 598 mas since 1977 (McAlister and Hartkopf 1984). The observation was made on 3 April 1988, under a seeing condition of 2". The optimal integration time for this object
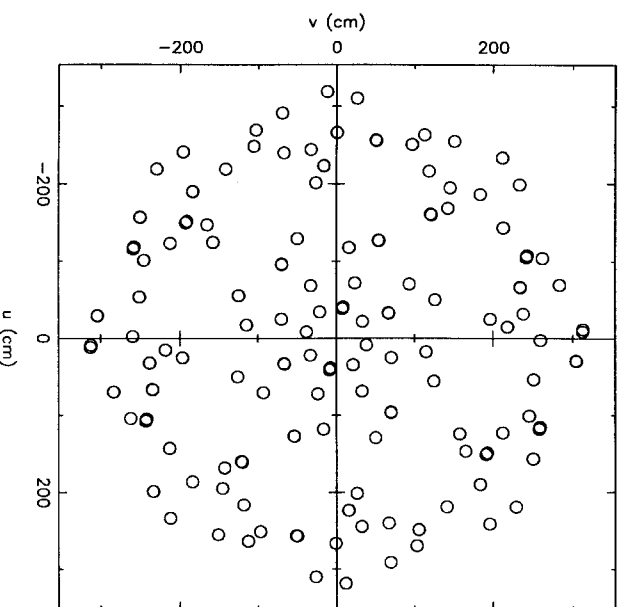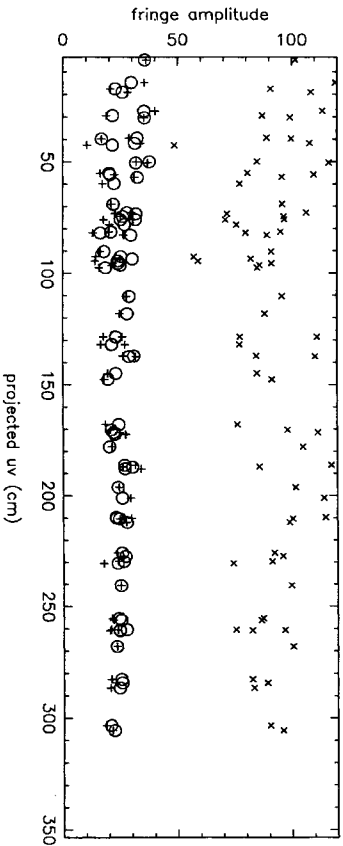

v (cm)

u (cm)

FIG. 5. *uv* coverage for the observation of σ Her. The unit is baseline length in centimeters.

FIG. 3. Raw fringe amplitudes of β CrB ($+$), raw fringe amplitudes of δ Boo (0), and calibrated amplitudes ($\times$) are plotted against the projected uv plane along the orientation of the binary.

FIG. 7. Reconstructed image of σ Her. Contour levels are -2%, -1%, 1%, 2%, 3%, 5%, 10%, 20%, 30%, 40%, 50%, and 60% of the maximum. The top is to the north and to the left is the east.

of β CrB and σ Her: the best-fit binary star model, the best-fit point-source model, a binary star model with an additional flux of 2% to the second component to the best-fit one, a binary star model with an additional flux of 5% to the second component, a triple star model whose third component of 2% is additional to the best-fit binary star model, and a triple star model whose third component of 5% is additional to the best-fit binary star model. In the triple star model, three components geometrically form an equilateral right triangle whose right-angle vertex is the primary component. Since the goodness of fit is primarily determined by the systematic errors, fitting parameters do not behave as Gaussian random variables and therefore it is not possible to estimate quantitatively the likelihood of models based on the χ^2 distribution. Here we interpret the combination of the degrees of freedom and χ^2 semiquantitatively.

In the case of β CrB, the best-fit point-source model is nowhere near the best-fit binary star model, while in the case of σ Her, the best-fit point-source model is not so far from the best-fit binary star model. This is because of the differ-

ence in the magnitude differences of the two binary stars. An additional component of 2% to the best-fit model of β CrB appreciably increases χ^2, while one to the best-fit model of σ Her affects χ^2 differently depending on where the additional component is. Apparently, a change of flux by 2% is not significant in the case of σ Her. On the other hand, an additional component of 5% causes a significant change in χ^2 in both of the cases. These support the estimate given in Sec. V that the dynamic range of the map of β CrB is 50:1 and that of σ Her is 30:1.

c) Fundamental Differences between Radio Interferometry and Nonredundant Masking

We now discuss some fundamental differences between radio interferometry and optical NRM. These differences are primarily in the order of correlations of observables, the behavior of signal-to-noise ratios of observables according to the light level, and interference-detection scheme of the light. Here the order of correlation of observables n is defined mathematically as the number of complex fringe amplitudes needed to define a particular observable. For instance, the order of correlation of the power spectrum or closure phase is two and that of the bispectrum or closure phase three. The behavior of the signal-to-noise ratios of observables depends on the order of correlation and the light level. At high light levels, the signal-to-noise ratios of both the fringe amplitude and closure phase are $\propto N^{1/2}$, where N is the number of photon events per coherent integration time. At low light levels, the signal-to-noise ratio of the fringe amplitude is $\propto N$, while that of the closure phase is $\propto N^{3/2}$. The general expression of signal-to-noise ratios of the power spectrum and the bispectrum as functions of the number of photons are obtained by Dainty and Greenaway (1979) and Nakajima (1988), respectively. Henceforth, the behavior of the signal-to-noise ratio of an observable is $\propto N^\alpha$, is specified by the "SNR exponent" α.

In most cases of radio interferometry, except for VLBI, both fringe amplitudes and phases or complex fringe amplitudes are observable. In the case of VLBI, observables are the fringe amplitude (second-order correlation) and the closure phase (third-order component) as in optical NRM. However, there is a difference in the behavior of the signal-to-noise ratios of the observables between radio VLBI and optical NRM.

In radio interferometry, one heterodyne receiver is associated with each antenna and the characteristics of the antenna-receiver combinations cause station-dependent errors. In NRM, the beams from all the holes (stations) are introduced to a two-dimensional incoherent detector where the quantum-me-

CLEAN MAP

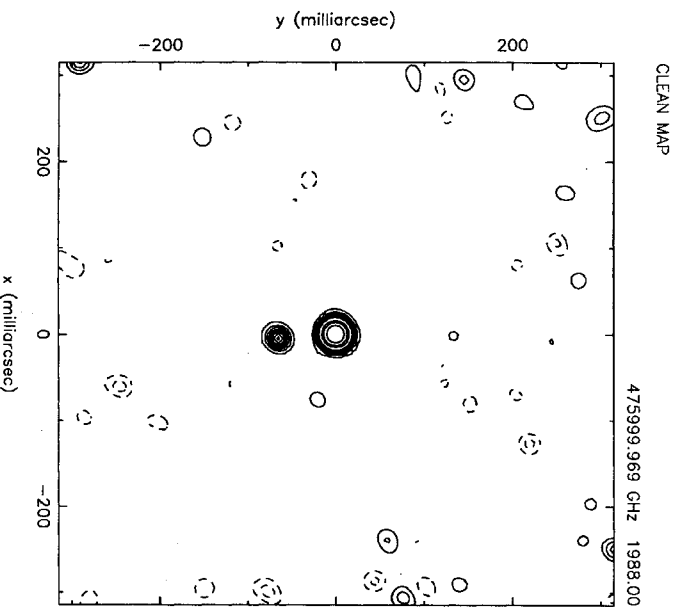475999.969 GHz   1988.00

y (milliarcsec)
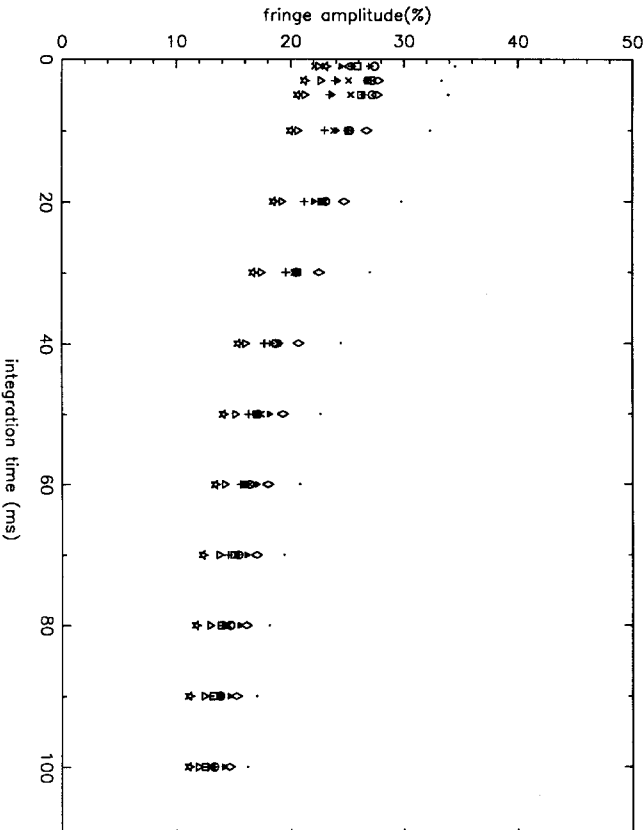
x (milliarcsec)

1989AJ.....97.1510N

FIG. 9. Raw fringe amplitudes of β CrB for the mask position angle of 36° are plotted against integration time. Ten different symbols denote fringe amplitudes of different baselines.

chanical interference of each photon takes place (e.g., Dirac 1958). The concept of a station becomes vague, since it is impossible to measure the wave function at each hole. Within a coherent integration time, there is only a sparse distribution of photon events which hardly looks like a fringe pattern. If it were not for the atmospheric disturbance, the fringe pattern or complex amplitude would become an observable from an ensemble of many photon events, since the classical fringe pattern would be a probability distribution for individual photons. Instead of the probability distribution, it is necessary because of the atmospheric disturbance to estimate the second- and third-order correlations of the probability distribution from ensembles of photon-event correlations. The necessity of higher-order correlations leads to a very low signal-to-noise ratio per coherent integration time and to the necessity of processing a large number of frames. The low signal-to-noise ratio per coherent integration time sets a limitation on the timescale of amplitude calibration. Four differences found in the practice of data reduction and analysis are discussed in the following.

d) Error in Closure Phase

At radio wavelengths, the amplitude uncertainty (A/σ_A) is related to the phase error σ_ϕ as

$$\sigma_\phi = A/\sigma_A, \tag{7}$$

since $\alpha(\text{fringe amplitude}) = \alpha(\text{fringe phase}) = \frac{1}{2}$. The error in the closure phase can then be estimated from the propagation of phase errors:

$$\sigma_{jkl}^2 = \sigma_{jk}^2 + \sigma_{kl}^2 + \sigma_{lj}^2, \tag{8}$$

since $\alpha(\text{fringe phase}) = \alpha(\text{closure phase}) = \frac{1}{2}$.

For an observation of a faint object at optical wavelengths, however, $\alpha(\text{fringe amplitude}) = 1$, the fringe phase is not observable, and $\alpha(\text{closure phase}) = \frac{3}{2}$. Therefore there is no simple relation between the amplitude error and the closure phase error.

TABLE II. χ^2 for different models of β CrB and σ Her. The first raw fit has the star name and the type of models. The second and third raw fits are degrees of freedom and χ^2, respectively. From the second column to the seventh column are the best-fit binary star model, the best-fit point-source model, a binary star model whose second component is increased by 2% of the maximum, a binary star model whose second component is increased by 5% of the maximum, a triple star model made from the best-fit binary star model by adding the third component of 2% of the maximum, and a triple star model made from the best-fit binary star model by adding the third component of 5% of the maximum. In the triple star model, the three components form an equilateral right triangle whose right-angle vertex is the primary component.

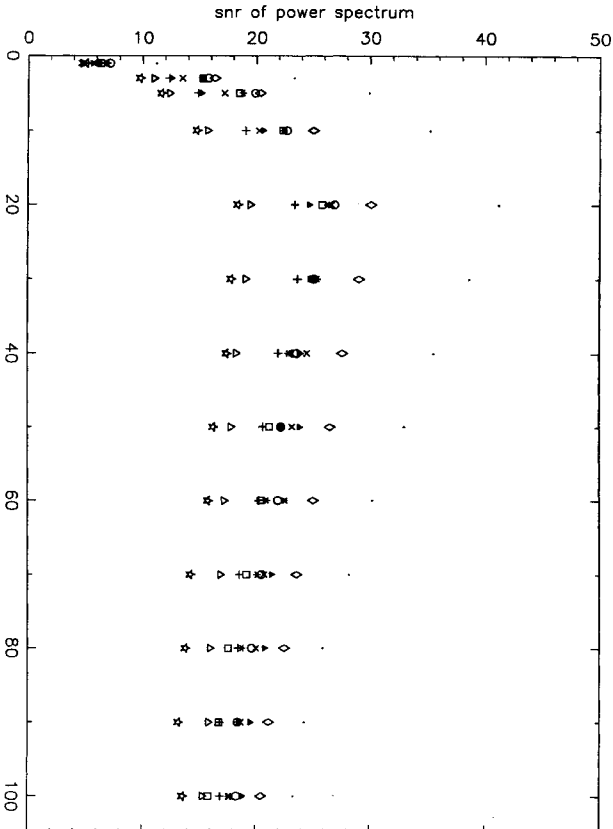| β CrB	best fit binary	best fit point	2nd+2%	2nd+5%	triple(3rd=2%)	triple(3rd=5%)
degrees of freedom	76	79			76	
χ^2	234	323	236	268	237	269
σ Her	best fit binary	best fit point	2nd+2%	2nd+5%	triple(3rd=2%)	triple(3rd=5%)
degrees of freedom	171	174			171	
χ^2	275	292	281	297	275	284

FIG. 10. Signal-to-noise ratios of power-spectrum components of β CrB for the mask position angle of 36° are plotted against integration time. The observed photon rate was 5.7 kHz; the total number of photons was about 1.2×10^5.

respectively. The signal-to-noise ratio of the power spectrum (or fringe amplitude) peaks at an integration time of 20 ms, while that of the bispectrum (or closure phase) has a broad peak between 20 and 60 ms. At this low photon rate (≈ 5 kHz), for a given dataset (the total number of photons fixed), the signal-to-noise ratio of the power spectrum is expected to be proportional to

$$V_\tau^2 \times \sqrt{\tau}, \qquad (9)$$

while that of the bispectrum is expected to be proportional to

$$V_\tau^3 \times \tau, \qquad (10)$$

where τ is the integration time and V_τ is the fringe amplitude as a function of τ (see the Appendix). Therefore a longer

e) Optimal Integration Times for Amplitude and Closure Phase

Since α(fringe amplitude) $\neq \alpha$(closure phase), we do not necessarily expect the same optimal integration time ($\tau \propto N$) for these two quantities. One advantage of using a photon-counting detector is in that the effect of the atmospheric disturbance can be traced as a function of coherent integration time τ. In Fig. 9, fringe amplitudes of β CrB at a position angle of the mask of 36° are plotted against τ. A slow decay of fringe amplitudes indicates good seeing conditions. Fringe amplitudes of the calibrator showed a very similar decay pattern, which was necessary for a successful amplitude calibration. Signal-to-noise ratios of the power spectrum and the bispectrum are plotted as functions of τ in Figs. 10 and 11,
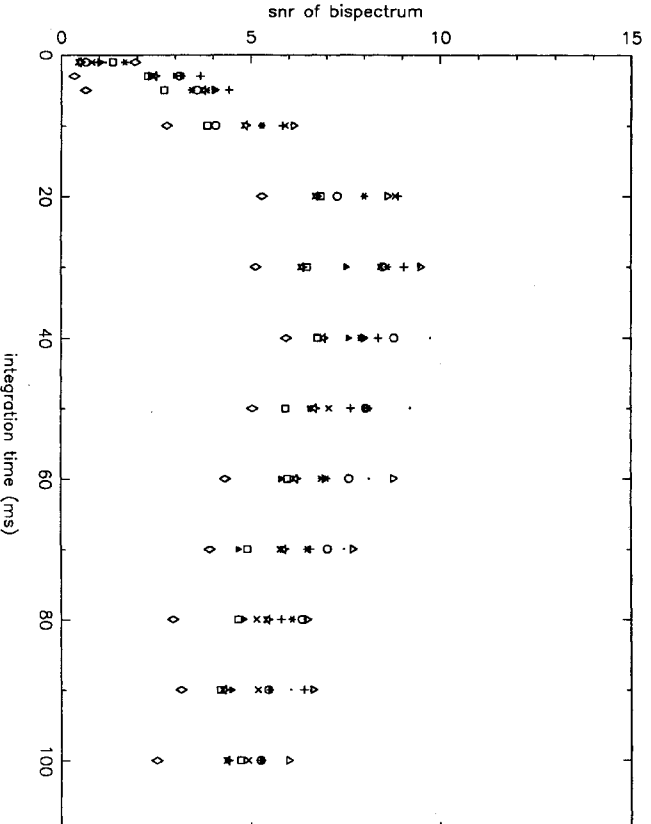

FIG. 11. Signal-to-noise ratios of bispectrum components of β CrB for the mask position angle of 36° are plotted against integration time. Different symbols denote different triangles. The observed photon rate was 5.7 kHz; the total number of photons was about 1.2×10^5.

optimal coherent integration time for the bispectrum is expected at a low photon rate. As the light level is lowered, the discrepancy of the optimal integration time for the power spectrum and that for the bispectrum becomes wider. Since the peak of the signal-to-noise ratio of the bispectrum was broad, both the power spectrum and bispectrum were calculated with an integration time of 20 ms for all the datasets taken at different rotational angles of the mask. However, the choice of separate integration times for the amplitude and the closure phase should be considered in observing fainter objects.

f) Absence of Primary-Beam Correction

Unlike the case in radio aperture synthesis, there is no primary-beam correction in the optical NRM method. The "primary-beam correction" is a sensitivity correction made when the field of view of the synthesized map is comparable to the primary-beam size of each radio antenna.

A variation of gain within a field of view occurs because each radio antenna is accompanied by a single heterodyne detector which is sensitive to only one angular mode (λ/D). In the case of the optical NRM, all the beams from different holes (stations) on the mask are combined onto a two-dimensional incoherent detector plane where no variation in sensitivity is seen in principle. Therefore, there is no primary-beam correction at optical wavelengths. In practice, a finite bandwidth and physical dimension of the detector limits the field of view. The finite-bandwidth effect on the field of view θ_{FW} is estimated by the relation

$$\theta_{FW} \sim \frac{\lambda}{\Delta\lambda}\frac{\lambda}{D}.$$ (11)

For the observations of binary stars presented in this paper, $\theta_{FW} > 600$ mas and the effect is negligible.

g) Difficulty in Amplitude Self-Calibration

In radio VLBI, two methods of amplitude self-calibration, "closure amplitude" (Readhead et al. 1980) and the method of Cornwell and Wilkinson (1981), are successfully used. Although the two methods are different in approaches, both of them require certain signal-to-noise ratios of closure amplitudes or complex fringe amplitudes within each coherent integration time and the absence of significant baseline-dependent errors. Self-calibration is reviewed by Pearson and Readhead (1984, and references therein).

At optical wavelengths, the signal-to-noise ratio of a fringe amplitude per coherent integration time is typically very low (<0.3), because of photon noise. A closure amplitude formed by four fringe amplitudes has much lower signal-to-noise ratio than each amplitude and is not practically measurable even after integrating over many frames. The method of Cornwell and Wilkinson is not applicable either within this short timescale. Realistically, there is no amplitude calibration within the timescale of coherent integration.

At optical wavelengths, amplitude self-calibration must be attempted in a timescale of many coherent integrations in order to eliminate photon noise compared to other systematic errors. For the observations reported in this paper, this timescale was on the order of several minutes. After the elimination of photon noise, time-averaged amplitudes may include both static or long-term systematic errors and short-term errors. A closure amplitude formed by four time-averaged fringe amplitudes cancels out long-term station-dependent errors. The quality of the "long-term closure amplitudes" of the point-source calibrator for β CrB, δ Boo, was examined by comparing them with "fake closure amplitudes" formed by nonclosed combinations of two random amplitudes in the numerator and two others in the denominator. It was found to be poor, showing that the errors of the fringe amplitudes were dominated by short-term station-dependent errors and/or baseline-dependent errors.

A fairly good calibration of the amplitudes of β CrB by dividing those of δ Boo suggested that the atmospheric condition was rather stable during the observation of the pair of stars (Sec. V). For this particular period, the amplitude errors must have been dominated by static or long-term errors. Combined with the poor "long-term closure amplitudes" of δ Boo, the successful division indicated the significance of static or long-term baseline-dependent errors. The presence of baseline-dependent errors reduces the effectiveness of the method of Cornwell and Wilkinson applied to a long timescale. It has been found by Monte Carlo simulations of the effect of the atmospheric disturbance on the NRM based on the Kolmogorov spectrum that the reduction of the fringe amplitude by the refractive effect of the atmospheric disturbance is a major cause of long-term baseline-dependent errors (Nakajima et al. 1989). Astigmatism of the primary mirror is one of the suspected causes of static baseline-dependent errors.

VII. CONCLUSIONS

We have carried out an experiment of optical aperture-synthesis imaging using the nonredundant masking technique at the Hale 5 m telescope. Reduced observables, amplitudes, and closure phases were processed by the Caltech VLBI hybrid-mapping package. Our main conclusions are summarized below.

Images of two bright binary stars were successfully constructed. β CrB, with a separation of 230 milliarcsec, was resolved by a 50 milliarcsec beam. The dynamic range of the image was 50:1. σ Her, with a separation of 70 milliarcsec, was resolved by a 30 milliarcsec beam. The dynamic range of the image was 30:1. The results demonstrate the potential of the technique for diffraction-limited imaging of astronomical objects with high dynamic range.

In the data reduction, the optimal coherent integration times for the fringe amplitude and the closure phase are not necessarily the same, since the signal-to-noise ratios of these quantities behave differently according to the integration time. In general, the optimal integration time for the closure phase is longer than that for the fringe amplitude.

The direct application of the radio-imaging technique worked well as a starting point for optical aperture synthesis. However, there are some major differences between optical and radio regimes, which leave room for improvement of optical imaging.

At optical wavelengths, amplitude calibration is applied only to average fringe amplitudes over many coherent integration times and is not effective in correcting short-term variations of the atmosphere. Unlike in radio interferometry, significant baseline-dependent errors were found in our experiment. A close relation between amplitude errors and phase errors seen at radio wavelengths does not exist at optical wavelengths. As a result, one important function of the hybrid-mapping procedure, amplitude self-calibration, does not have the basis for effectiveness at optical wavelengths.

These facts are to be taken into account in future algorithms for optical aperture-synthesis imaging.

Primary-beam correction of radio interferometry is not necessary in optical aperture synthesis, due to the incoherent detection scheme at optical wavelengths.

APPENDIX: SIGNAL-TO-NOISE RATIO VERSUS INTEGRATION TIME

The power spectrum and bispectrum analysis of images affected by photon noise are well understood in terms of the behavior of the signal-to-noise ratio according to the light level (Goodman and Belsher 1976, 1977; Dainty and Greenaway 1979; Wirnitzer 1985; Nakajima 1988), including the covariance analysis (Kulkarni and Nakajima 1989). In this Appendix, these results are applied to photon-noise-limited fringe patterns.

Here the dependence of the signal-to-noise ratio of the power spectrum and that of the bispectrum on the integration time and the fringe amplitude, Eqs. (9) and (10), are derived at low light levels. The discussion given here can easily be generalized to arbitrary light levels using the expression for the signal-to-noise ratio of the power spectrum per short-exposure frame (Dainty and Greenaway 1979) and that of the bispectrum (Nakajima 1988). It can also be generalized to a covariance analysis to obtain the number of statistically independent fringe amplitudes and statistically independent closure phases (Kulkarni and Nakajima 1989).

At low light levels, the signal-to-noise ratio per short-exposure frame of the power-spectrum component at spatial frequency $\mathbf{u}$ is given by

$$\bar{N} \langle |\tilde{i}(\mathbf{u})|^2 \rangle,$$ (A1)

where $\bar{N}$ is the number of photons per frame, $\langle \ \rangle$ stands for an ensemble average, and $|\tilde{i}(\mathbf{u})|^2$ is the power-spectrum component normalized by the zero-spatial-frequency component (Dainty and Greenaway 1979). The signal-to-noise ratio of the bispectrum component at $(\mathbf{u}_1, \mathbf{u}_2)$ is given by

$$\bar{N}^{3/2} \langle |\tilde{b}^{(3)}(\mathbf{u}_1, \mathbf{u}_2)| \rangle,$$ (A2)

where $\tilde{b}^{(3)}(\mathbf{u}_1, \mathbf{u}_2)$ is the bispectrum component (Wirnitzer 1985; Nakajima 1988).

In the case of the NRM, each power-spectrum component is related to the fringe amplitude V_τ as

$$\langle |\tilde{i}(\mathbf{u})|^2 \rangle = \frac{V_\tau^2}{n_s^2},$$ (A3)

where V_τ is the fringe amplitude as a function of the integration time and n_s is the number of holes. A bispectrum component is given by

$$\langle \tilde{b}^{(3)}(\mathbf{u}_1, \mathbf{u}_2) \rangle = \frac{\langle v_1 v_2 v_3 \rangle}{n_s^3},$$ (A4)

where $v_1 v_2 v_3$ is the triple product of three complex visibilities. In the case of a point source, or a binary star with a large magnitude difference ($\Delta m \gg 1$),

$$|\langle v_1 v_2 v_3 \rangle| \approx V_\tau^3,$$ (A5)

since the closure phase is zero or small.

For a dataset with the total number of photons N_{tot}, the signal-to-noise ratio of the integrated power spectrum S_P is given by

$$S_P = \frac{\bar{N}}{n_s^2} V_\tau^2 \sqrt{\frac{N_{tot}}{N}} = \sqrt{\frac{RN_{tot}}{n_s^2}} \ V_\tau^2 \sqrt{\tau},$$ (A6)

where R is the photon rate and thus $\bar{N} = R\tau$. The signal-to-noise ratio of the integrated bispectrum S_B is given by

$$S_B = \bar{N}^{3/2} \frac{V_\tau^3}{n_s^3} \sqrt{\frac{N_{tot}}{N}} = \frac{R\sqrt{N_{tot}}}{n_s^3} V_\tau^3 \tau,$$ (A7)

It is intuitively clear that the S_P and S_B peak at different τ and that the optimal integration time for the power spectrum (or fringe amplitude) is shorter. A brief confirmation is given here.

$$\frac{d \log (S_P)}{d\tau} = 2 \frac{d \log V_\tau}{d\tau} + \frac{1}{2} \frac{1}{\tau},$$ (A8)

while

$$\frac{d \log (S_B)}{d\tau} = 3 \frac{d \log V_\tau}{d\tau} + \frac{1}{\tau}.$$ (A9)

S_P peaks when

$$2 \frac{d \log V_\tau^*}{d\tau} + \frac{1}{2} \frac{1}{\tau^*} = 0$$ (A10)

and

$$3 \frac{d \log V_\tau^*}{d\tau} + \frac{1}{\tau^*} = -\frac{d \log V_\tau^*}{d\tau},$$ (A11)

where * stands for a value at the peak of S_P. Since V_τ is a monotonically decreasing function of τ, $-(d \log V_\tau^*/d\tau)$ is positive. Therefore, when S_P peaks at a given τ^*, S_B is still increasing.

REFERENCES

Cornwell, T. J., and Wilkinson, P. N. (1981). Mon. Not. R. Astron. Soc. 196, 106.
Dainty, J. C., and Greenaway, A. H. (1979). J. Opt. Soc. Am. 69, 786.
Dirac, P.A.M. (1958). The Principles of Quantum Mechanics, 4th ed. (Oxford University, Oxford).
Goodman, J. W., and Belsher, J. F. (1976). Tech. Rep. RADC-TR-76-50, RADC-TR-76-382 (Rome Air Development Center, New York).
Goodman, J. W., and Belsher, J. F. (1977). Tech. Rep. RADC-TR-77-175 (Rome Air Development Center, New York).
Gorham, P. W., Ghez, A. M., Kulkarni, S. R., Nakajima, T., Neugebauer, G., Oke, J. B., Prince, T. A., and Readhead, A. C. S. (1989). In preparation.
Haniff, C. A., Mackay, C. D., Titterington, D. J., Sivia, D., Baldwin, J. E., and Warner, P. J. (1987). Nature 328, 694.

Hoffeit, D., and Jaschek, C. (1982). *The Bright Star Catalog*, 4th ed. (Yale University Observatory, New Haven).

Hofman, K.-H., and Weigelt, G., (1986). Astron. Astrophys. **167**, L15.

Högbom, J. A. (1974). Astron. Astrophys. Suppl. **15**, 417.

Knox, K. T., and Thompson, B. J. (1974). Astrophys. J. Lett. **193**, L45.

Kulkarni, S. R. (1988a). In *Proceedings of the Joint ESO/NOAO Conference on High-Resolution Imaging by Interferometry*, edited by F. Merkle (ESO, Garching), p. 595.

Kulkarni, S. R. (1988b). Preprint, California Institute of Technology.

Kulkarni, S. R., and Nakajima, T. (1989). In preparation.

Labeyrie, A. (1972). Astron. Astrophys. **6**, 85.

McAlister, H. A., and Hartkopf, W. I. (1984). *Catalog of Interferometric Measurements of Binary Stars* (Center for High Angular Resolution Astronomy, Georgia State University, Atlanta).

Nakajima, T. (1988). J. Opt. Soc. Am. A **5**, 1477.

Nakajima, T., Kulkarni, S. R., and Readhead, A. C. S. (1989). In preparation.

Nisenson, P., Stachnik, V., Karovska, M., and Noyes, R. (1985). Astrophys. J. Lett. **297**, L17.

Pearson, T. J., and Readhead, A. C. S. (1984). Annu. Rev. Astron. Astrophys. **22**, 97.

Readhead, A. C. S., Nakajima, T., Pearson, T. J., Neugebauer, G., Oke, J. B., and Sargent, W. L. W. (1988). Astron. J. **95**, 1278 (Paper I).

Readhead, A. C. S., Walker, R. C., Pearson, T. J., and Cohen, M. H. (1980). Nature **285**, 137.

Readhead, A. C. S., and Wilkinson, P. N. (1978). Astrophys. J. **223**, 25.

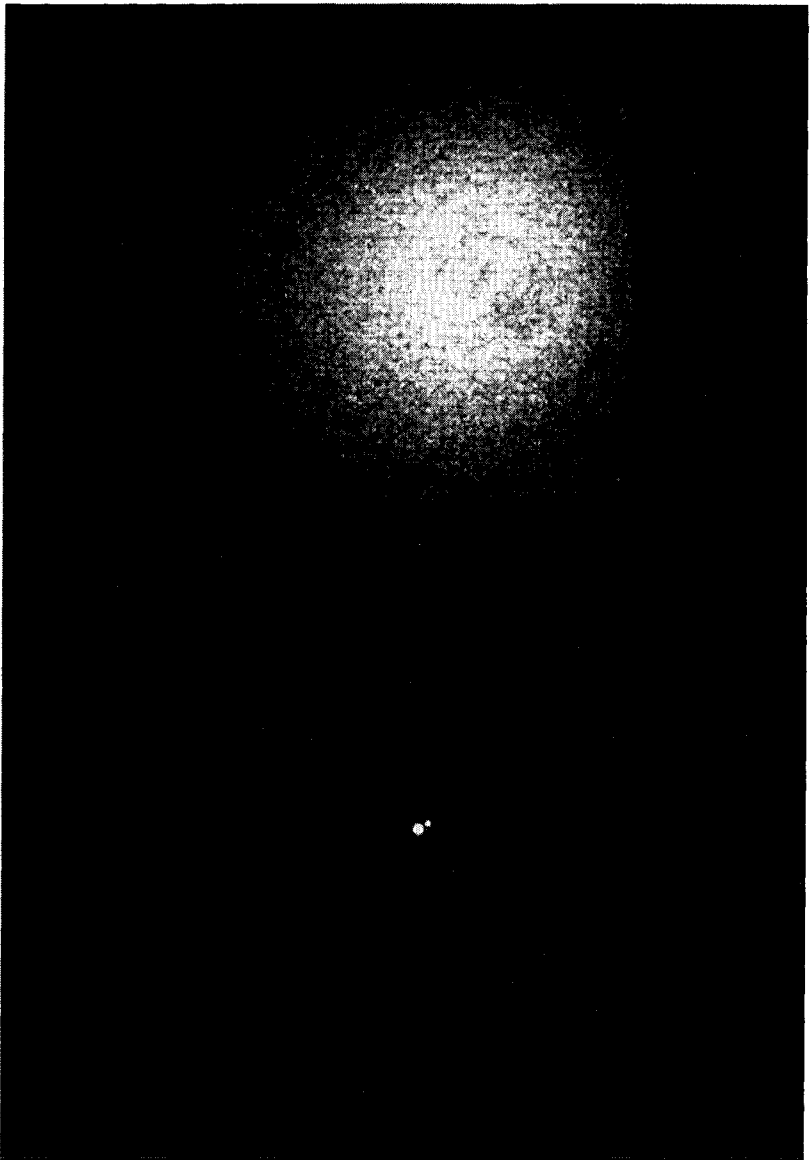Wirnitzer, B. (1985). J. Opt. Soc. Am. A **2**, 14.

FIG. 8. A long time exposure (left) and the constructed image (right) of a binary star, σ Herculis, in the same scale. The seeing-disk diameter is about 2 arcsec, while the separation of the binary star is 70 milliarcsec.

Nakajima *et al.* (see page 1514)